Fermi-type particle acceleration from magnetic reconnection at the termination shock of a relativistic striped wind

Yingchao Lu,[1,2,*] Fan Guo,[2] Patrick Kilian,[2] Hui Li,[2] Chengkun Huang,[2] and Edison Liang[1]

[1] *Department of Physics and Astronomy, Rice University, Houston, Texas 77005, USA*
[2] *Theoretical Division, Los Alamos National Laboratory, Los Alamos, New Mexico, 87545, USA*

(Dated: February 1, 2022)

An oblique-rotating pulsar generates a relativistic striped wind in a pulsar wind nebula (PWN). The termination shock of the PWN compresses the Poynting-flux-dominated flow and drives magnetic reconnection. By carrying out particle-in-cell (PIC) simulations of the termination shock of the PWN, we study the shock structure as well as the energy conversion processes and particle acceleration mechanisms. With the recent advances in the numerical methods, we extend the simulations to the ultra-relativistic regime with bulk Lorentz factor up to $\gamma_0 = 10^6$. Magnetic reconnection at the termination shock is highly efficient at converting magnetic energy to particle kinetic energy and accelerating particles to high energies. We find that the resulting energy spectra crucially depend on λ/d_e. When λ/d_e is large ($\lambda \gtrsim 40d_e$) , the downstream particle spectra form a power-law distribution in the magnetically dominated relativistic wind regime with upstream magnetization parameter $\sigma_0 = 10$. By analyzing particle trajectories and statistical quantities relevant to particle energization, we find that Fermi-type mechanism dominates the particle acceleration and power-law formation. We find that the results for particle acceleration are scalable as γ_0 and σ_0 increase to large values. The maximum energy for electrons and positrons can reach hundreds of TeV if the wind has a bulk Lorentz factor $\gamma_0 \approx 10^6$ and magnetization parameter $\sigma_0 = 10$, which can explain the recent observations of high-energy gamma-rays from pulsar wind nebulae (PWNe).

I. INTRODUCTION

A rotating pulsar creates the surrounding pulsar wind nebula (PWN) by steadily releasing an energetic wind into the interior of the expanding shockwave of a core-collapse supernova explosion [1]. The wind is composed of magnetized plasma of relativistic electrons and positrons. The wind propagates radially and abruptly transits at the termination shock where the ram pressure balances that of the surrounding medium (supernova remnant or interstellar medium depending on the age and motion of the PWN [1, 2]). The wind can transit from being Poynting-dominated to being particle-dominated at the termination shock. Particles in the pulsar wind will be accelerated at the termination shock, producing a broadband spectrum that can be observed from the radio to X-ray bands. The spectral breaks between the radio and the X-ray band have been found in the synchrotron spectra of pulsar wind nebulae (PWNe). Some of the spectral breaks suggest emission processes fed by non-thermal particle distributions at the termination shock [3–5]. How the electromagnetic energy is converted into particle energy and how non-thermal particles are efficiently accelerated at the termination shock is not fully understood.

Recently, high-energy gamma-ray emissions have been detected in both young PWNe and mid-aged PWNe. The Crab nebula (about 10^3 years old, and the Crab pulsar has spin-down luminosity $\dot{E} \sim 5 \times 10^{38}$erg/s) is a prototype of young and energetic PWNe. The origin of the observed photons of energy $E_{\rm ph} > 100$ TeV from the Crab is likely due to the acceleration of leptons in the vicinity of PeV in the Crab nebula [6, 7]. The ultra-high-energy electrons and positrons can be produced by particle acceleration in the nebula [8]. Mid-age pulsars such as Geminga (more than 10^5 years old, $\dot{E} \sim 3 \times 10^{34}$erg/s) are beyond the synchrotron cooling time, but still accelerate electrons to very high energies in the nebulae [9]. In a recent survey [10], nine Galactic sources are found to emit above 56 TeV with data from High Altitude Water Cherenkov (HAWC) Observatory, eight of which are within a degree of the Galactic plane (the ninth source is the Crab Nebula). Those eight inner Galactic plane sources are associated with high spin-down pulsars ($\dot{E} \gtrsim 10^{36}$erg/s) and remain extended in apparent size above 56 TeV even though the gamma-ray radiating electrons cool quickly. How pulsar winds efficiently accelerate electrons and positrons to high energies is a major puzzle and holds the key of understanding the near-Earth positron anomaly [9, 11, 12] as well as gamma rays from the Galactic Center [9, 10, 13, 14].

In the case of an oblique-rotating pulsar, a radially propagating relativistic flow is continuously launched. Near the equatorial plane, toroidal magnetic fields of alternating polarity, separated by current sheets, are embedded in the flow. Such a flow has been modeled as a steady state striped wind, containing a series of drifting Harries current sheets [15, 16]. Numerical simulations including magnetohydrodynamics (MHD) [5, 17–19], particle-in-cell (PIC) [20] and test-particle simulations [21] have been used to model the termination shock of PWNe. However, how magnetic energy is converted, and the role of the termination shock [22–24] and relativistic magnetic reconnection [25–29] in accelerating par-

* yingchao.lu@rice.edu

ticles is still unclear [2]. Magnetic reconnection driven by the termination shock may dissipate the magnetic energy and accelerate particles [20, 30].

Particle acceleration in relativistic magnetic reconnection has been a recent topic of strong interests. In the case of a spontaneous reconnection, controversy on the role of direct acceleration and Fermi acceleration in producing the power-law particle energy distribution has been extensively addressed [25–27]. Sironi and Spitkovsky [26] have suggested that the power-law forms as the particles interact with the X-points (diffusion regions with weak magnetic field $|\boldsymbol{E}| > |\boldsymbol{B}|$) through direct acceleration. In contrast, analyses by Guo et al. [25, 27, 29] show that the power-law distributions are produced by Fermi-like processes and continuous injection from the reconnection inflow. In the case of the shock-driven reconnection at the termination shocks of highly relativistic striped pulsar winds, Sironi and Spitkovsky [20] have proposed that high-energy particles are mainly accelerated at the electric fields at the X-points. However, the role of Fermi-like processes have not been studied in the shock-driven reconnection systems, which is a main focus of this paper.

In this paper, we employ 2D PIC simulations to model the relativistic striped wind interacting with the termination shock near the equatorial plane of obliquely rotating pulsars. We focus on studying the dynamics in a local box near the termination shock of the wind. While it is extremely difficult to model the macroscopic system due to the enormous scale separation between the system size and the skin depth, PIC models provide a reliable and self-consistent description of the shock structure, magnetic reconnection and particle acceleration. We find that the magnetic reconnection driven by the precursor perturbation from the shock converts the magnetic energy into particle energy and accelerates particles forming a power-law energy spectrum. We examine a wide range of bulk Lorentz factor $10^2 \leq \gamma_0 \leq 10^6$ and magnetization parameter $10 < \sigma_0 \equiv B_0^2/(4\pi\gamma_0 m_e n_{c0} c^2) < 300$ (assuming uniform magnetic field strength B_0 and uniform electron+positron density n_{c0} in the upstream) and show the scaling of the particle spectrum. Most of our simulations have large γ_0 well above the range $3 < \gamma_0 < 375$ used in previous simulations [20]. This is made possible using the recent improvement [31] of the PIC method to overcome the numerical problems. The wide range of γ_0 and σ_0 is expected for PWNe with various pulsar spin-down luminosity and age. Our analysis of the particle trajectories and particle energization terms shows that Fermi-type mechanisms by magnetic reconnection [29, 32] dominate the particle acceleration and power-law formation.

The rest of this paper is organized as follows. In Section II, we discuss the numerical methods and the setup of our simulations. In Section III, we discuss the evolution and structure of the shock-reconnection system for the standard run. In Section IV, we study the particle spectrum and its dependency on parameters γ_0, σ_0 and λ. In Section V, we give some detailed analyses of the particle acceleration mechanism. We discuss and conclude the paper in Section VI.

II. NUMERICAL SIMULATIONS

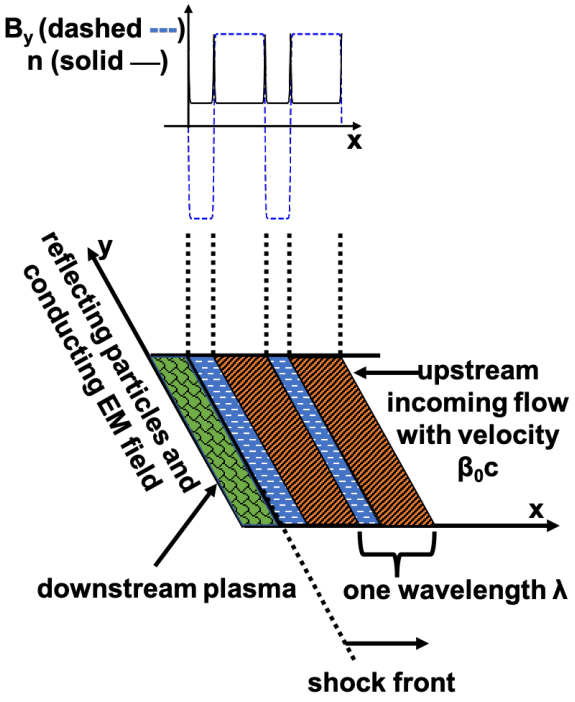

Figure 1. 2D PIC simulation setup for the termination shock of relativistic striped wind. The upstream incoming flow drifts with bulk Lorentz factor γ_0 and is composed of in-plane magnetic field B_y in $+y$ or $-y$ direction, and particles (electrons and positrons). In each current sheet, there is a hot dense component of particles as shown in the density profile. The hot component balances the magnetic pressure and ensures the steady electromagnetic profile.

We use the 2D version of PIC code EPOCH [33] to study the structure and physical processes in the termination shock of a relativistic striped wind. Overcoming numerical problems, especially the numerical Cherenkov instability (NCI) [34], is critical for correctly modeling highly relativistic plasma flows. To improve the numerical stability, we have heavily modified the code to implement the WT (standing for **w**eighting with **t**ime-step dependency) interpolation scheme [31], a piecewise polynomial force interpolation scheme with time-step dependency. This scheme eliminates the lowest order NCI growth rate and significantly suppresses growth from the residue resonances of higher orders by reducing time steps.

The spatial profile of the relativistic striped wind in our simulations is shown in Figure 1. The steady electron-positron flow propagates along $-x$ direction with a bulk Lorentz factor γ_0 before interacting with the reflected

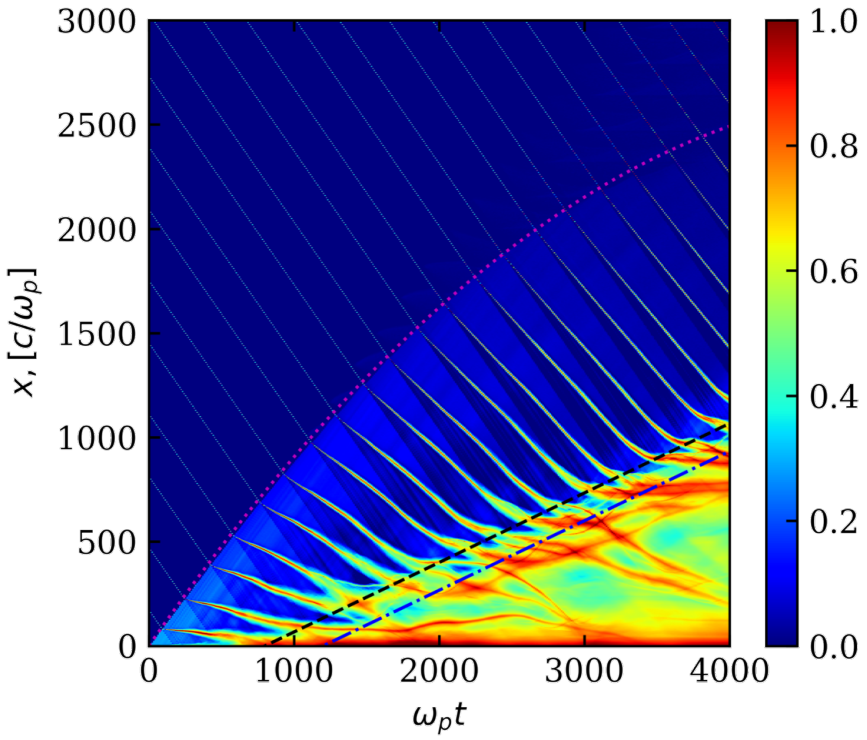

Figure 2. The evolution of density profile averaged over y direction, the variable plotted is $\log_{10}(\langle n\rangle_y/n_{c0})$. The magenta dotted line marks the location of the fast MHD shock (or the precursor perturbation). The expression for the location of the fast shock can be fitted as $x = ct[1-\omega_p t/103^2]$. The transition region of the slow (main) shock is between the black dashed line and the blue dot-dashed line. The expression for the transition region is $(ct-1200c/\omega_p)/3 < x < (ct-800c/\omega_p)/3$.

Table I. Parameters for each run in this work. The parameters listed are the transverse box size L_y, the wave length of the striped wind λ, upstream bulk Lorentz factor γ_0, the thickness of the current sheets Δ and the upstream magnetization σ. The lengths are in the unit of skin depth d_e.

Run	L_y/d_e	λ/d_e	γ_0	Δ/d_e	σ
S0	400	640	10^4	1	10
A1	400	640	10^2	1	10
A2	400	640	10^3	1	10
A3	400	640	10^5	1	10
A4	400	640	10^6	1	10
B1	$400\sqrt{3}$	$640\sqrt{3}$	10^4	$\sqrt{3}$	30
B2	$400\sqrt{10}$	$640\sqrt{10}$	10^4	$\sqrt{10}$	100
B3	$400\sqrt{30}$	$640\sqrt{30}$	10^4	$\sqrt{30}$	300
C1	400	160	10^4	1	10
C2	400	40	10^4	1	10
C3	400	20	10^4	1	10

flow. The spatial profile of the electromagnetic field in the simulation frame is

$$B_y = B_0 \tanh\left\{\frac{1}{\delta}\left[\alpha+\cos\left(\frac{2\pi(x+\beta_0 ct)}{\lambda}\right)\right]\right\} \quad (1)$$

$$E_z = \beta_0 B_0 \tanh\left\{\frac{1}{\delta}\left[\alpha+\cos\left(\frac{2\pi(x+\beta_0 ct)}{\lambda}\right)\right]\right\} \quad (2)$$

where β_0 is the velocity of the wind normalized by the speed of light c, and λ is the wavelength of the stripes in the wind. The dimensionless parameters δ and α are such that the half thickness of the current sheet is $\Delta = \lambda\delta/(2\pi)$, and B_y averaged over one wavelength is $\langle B_y\rangle_\lambda = B_0[1-2(\arccos\alpha)/\pi]$. The background cold plasma in the wind is uniform, with constant density $n^{\rm cold}_{e^-,e^+} = n_{c0}/2$ and constant temperature $kT^{\rm cold}_{e^-,e^+} = 0.04mc^2$ for both electrons and positrons. The time in our simulations is normalized by $1/\omega_p$ where $\omega_p = \sqrt{4\pi n_{c0}e^2/(\gamma_0 m_e)}$ is the plasma frequency, and the spatial coordinates in our simulation are normalized by $d_e = c/\omega_p$. A hot electron-positron plasma inside the Harris current sheets balances the magnetic pressure and maintains the steady profile of electromagnetic field. The density of the hot electron-positron plasma in the current sheet in the simulation frame is

$$n^{\rm hot}_{e^-,e^+} = \frac{n_{h0}}{2\cosh^2\left\{\frac{1}{\delta}\left[\alpha+\cos\left(\frac{2\pi(x+\beta_0 ct)}{\lambda}\right)\right]\right\}} \quad (3)$$

where $n_{h0}/n_{c0} = \eta$ is the over-density factor relative to the cold particles outside the layer, and is set to be $\eta = 3$ [16, 20, 26]. The drift velocity in z direction of the hot particles is setup to ensure the steady profile of electromagnetic field, i.e. in the rest frame of the wind $\nabla \times \boldsymbol{B} = (4\pi/c)\boldsymbol{J}$ is satisfied everywhere so that the electric field stays zero. The left boundary located at $x = 0$ is reflecting for particles and conducting for electromagnetic fields. The shock is self-consistently generated by the interaction between the reflected flow and the incoming flow. Our simulations are performed in the downstream frame, where the resulting downstream plasma bulk flow is at rest when the shock is well developed and separated from the boundary. The simulation is periodic in the y direction. The length of the simulation box in the y direction is $L_y = 400d_e$ for the standard run S0, which is large enough to hold the largest island in the simulation and we have tested that a larger length in y direction does not change our main conclusions. In our standard run, we have $\alpha = 0.1$ (i.e. $\langle B_y \rangle_\lambda = 0.064B_0$), $\Delta = d_e$, $\lambda = 640d_e$, $\gamma_0 = 1/\sqrt{1-\beta_0^2} = 10^4$ and $\sigma_0 = B_0^2/(4\pi\gamma_0 m_e n_{c0} c^2) = 10$, and d_e is resolved with 7.5 computational cells. We use 4th order particle shape, which significantly reduce the numerical noise even for a relatively small number of particle per cell. Each computational cell is initialized with two electrons and two positrons in the cold wind, and additional two electrons and two positrons in the current sheets. The parameters for other runs with different γ_0 and σ_0 are listed in Table I, while the resolution and α remain same for all the runs. We have also performed limited experiments with higher resolutions, obtaining essentially the same results.

To ensure that the onset of reconnection is independent of numerical effects, we have extensively tested the stability of current sheets in a double-periodic simulation without the reflecting wall. The results using WT scheme [31] are summarized in Appendix A. It shows that the case with time step $\Delta t = 0.2\Delta t_{\rm CFL}$ can make sure that the onset of reconnection is much later than $\omega_p t = 2000$, which is roughly the longest time it takes for the shock to compress a current sheet in our simulation. Therefore, we choose $\Delta t = 0.2\Delta t_{\rm CFL}$ for all runs in this paper (see Table I).

III. SHOCK FORMATION AND EVOLUTION

In Figure 2, we show the evolution of density profile averaged over the y direction. In Figure 3, we show the 2D spatial distribution of density $\log_{10}(n/n_{c0})$, magnetic energy density over particle energy density $\log_{10}(\varepsilon_B/\varepsilon_P)$, averaged particle kinetic energy γ/γ_0, and particle energization rate $\boldsymbol{J}\cdot\boldsymbol{E}$ at $\omega_p t = 2000$. The shock-reconnection system forms and evolves self-consistently as the reflected plasma interacts with the incoming flow. During this initial process we observe a precursor perturbation, which is actually a fast shock, propagates towards the upstream side of the simulation box, compresses and decelerates the incoming currents sheets. This drives the magnetic reconnection because the perturbed and compressed current sheets are subject to rapid growth of the tearing instability. Magnetic reconnection rapidly converts magnetic energy into particle kinetic energies as current sheets evolve. This is further facilitated by the compression at the main shock layer, characterized by a huge density increase. The general shock and reconnection dynamics of our standard run S0 are similar to the previous study [20], where a fast shock (the precursor perturbation) and a slow hydrodynamic shock (main shock) are identified.

The fast shock travels close to the speed of light initially and slows down when interacting with the incoming flow afterwards, as tracked by the magenta dotted trajectory in Figure 2. The location of the precursor can be fitted as $x = ct[1-\omega_p t/103^2]$, with the region with larger x being unperturbed. The jump at the fast shock is sharp in the beginning and becomes smoother after it encounters more current sheets. The incoming current sheets are slowed down and compressed as they pass through the fast shock. As shown in Figure 3(b), the ratio of magnetic energy density to particle energy density $\varepsilon_B/\varepsilon_P$ in the regions between current sheets increases right after passing through the fast shock, indicating strong compression. As a result of the slowdown and weakening of the fast shock, a current sheet reaching the fast shock later gets slowed down less than the one reaching the fast shock earlier. More importantly, the fast shock compresses the current sheets, triggering the onset of fast reconnection (also see discussion below). There is a huge density jump at the main shock around $x_{\rm sh} \approx 354c/\omega_p$ at $\omega_p t = 2000$. The jump moves at a constant speed approximately $c/3$ (consistent with the jump condition of ultra-relativistic shock) in $+\hat{\boldsymbol{x}}$ direction as shown in Figure 3(a). This density jump can also be seen in Figure 2 between the black dashed line and the blue dot-dashed line, i.e. $(ct - 1200c/\omega_p)/3 < x_{\rm sh} < (ct - 800c/\omega_p)/3$.

Inside the transition region between the precursor and the slow shock, i.e. between the magenta dotted line and the black dashed line in Figure 2 or $354c/\omega_p \lesssim x \lesssim 1623c/\omega_p$ in Figure 3, the adjacent regions of opposite magnetic field polarity are pushed toward each other and reconnects. The current sheets continuously break into a series of magnetic islands separated by X-points. Strong energy conversion is associated with magnetic reconnection, resulting in small $\varepsilon_B/\varepsilon_P$ in the islands, as shown in 3(c). The islands coalesce, grow to larger sizes as they continuously move towards the downstream, and further grow after passing the main shock front. In the downstream, the average $\varepsilon_B/\varepsilon_P$ is around 0.3, much less than its initial value $\varepsilon_B/\varepsilon_P = 5$, indicating that most of the magnetic energy is converted to particle kinetic energy. As shown in Figure 3(c), the average particle Lorentz factor is $\langle\gamma\rangle \sim \gamma_0(1+\sigma_0) = 11\gamma_0$ in the downstream. The particles in the downstream can form thermal and nonthermal distributions, which will be discussed in Section IV. The energization rate $\boldsymbol{J}\cdot\boldsymbol{E}$, as plotted in Figure 3(d),

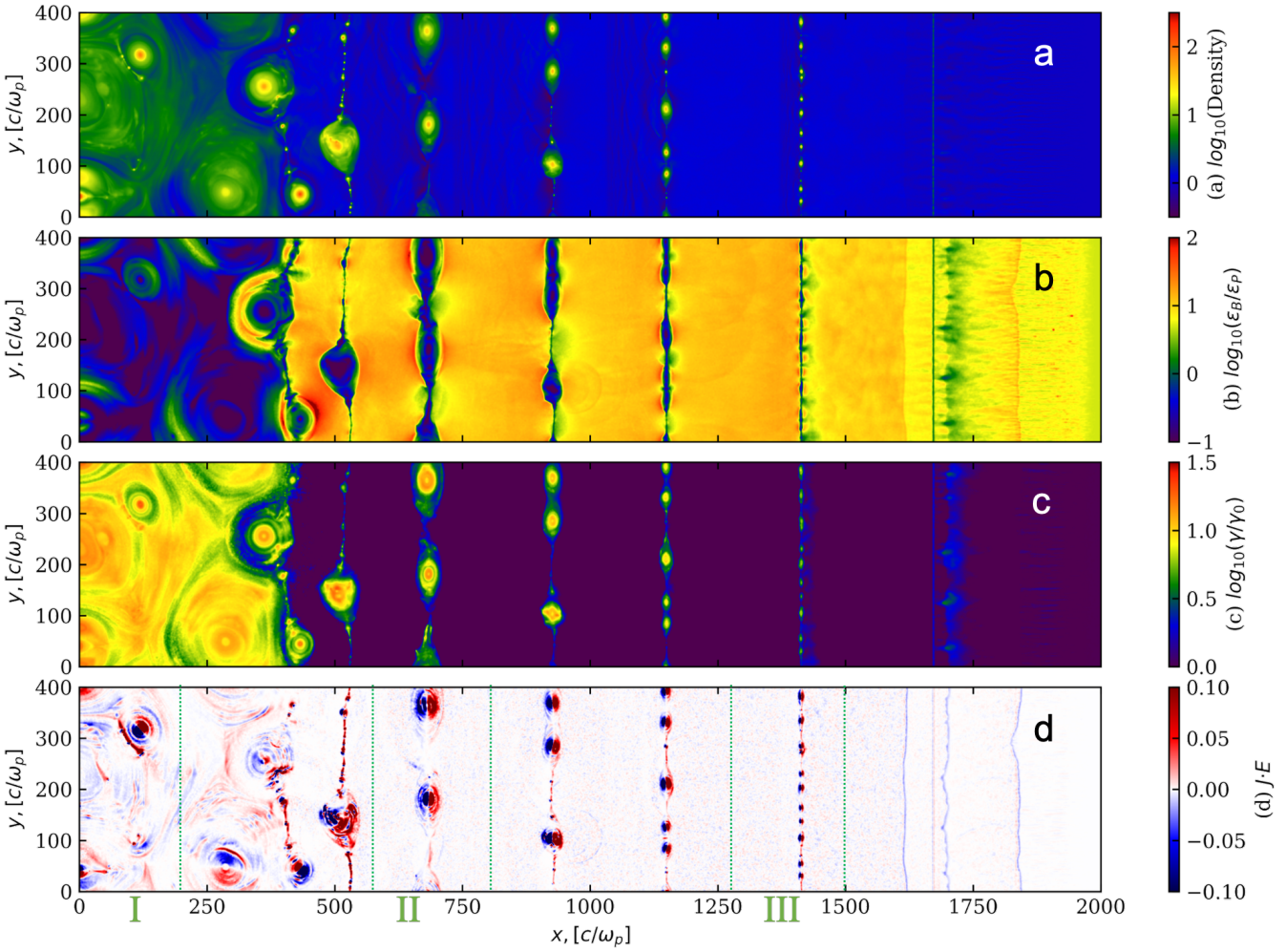

Figure 3. 2D spatial profile of different quantities for the standard run S0 with $\sigma_0 = 10$, $\gamma_0 = 10^4$, $\alpha = 0.1$ at time $\omega_p t = 2000$. (a) logarithm of particle number density normalized by n_{c0}, (b) logarithm of the ratio of magnetic energy density to particle energy density, (c) logarithm of average γ/γ_0, (d) energy conversion rate $\boldsymbol{J}\cdot\boldsymbol{E}$. The green dotted vertical lines are boundaries of regions for more detailed studies, region I for $0 < x/d_e < 197$, region II for $573 < x/d_e < 804$, and region III for $1275 < x/d_e < 1497$.

are concentrated in the current sheets and islands. More details about the energization will be discussed in Section V.

IV. PARTICLE SPECTRUM

As the shock forms and interacts with the current sheets embedded in the striped wind, the electrons and positrons are heated and accelerated. In Figure 4(a), we show the energy distribution function $f(\gamma)$ (related to the number distribution function $n(\gamma)$ by $f(\gamma) \equiv n(\gamma)\gamma$) in different regions for the standard run S0 at $\omega_p t = 2000$. Before reaching the fast shock, i.e. for $1600 < x/(c/\omega_p) < 2000$, $f(\gamma)$ has a peak at the bulk Lorentz factor $\gamma_0 = 10^4$. As the flow slows down, i.e. for $400 < x/(c/\omega_p) < 1600$, the peak of the spectrum shifts to a lower energy. As the current sheets reconnect, the tail of the spectrum becomes harder as the flow gets closer to the main shock. According to the jump condition, the averaged kinetic energy due to the energization in the downstream region is $\langle\gamma\rangle \approx \gamma_0(1+\sigma_0)$. For instance, in the standard run S0 ($\gamma_0 = 10^4$ and $\sigma_0 = 10$), we have $\langle\gamma\rangle \approx 1.1\times10^5$, which is consistent with the energy density for $0 < x/(c/\omega_p) < 400$ in Figure 4(a). However, the actual downstream particle spectrum is distinctly different from the thermal distribution. The particles with energies between $\gamma = 2\times10^4$ and $\gamma = 4\times10^5$ follow a power-law distribution $f(\gamma) \propto \gamma^{-p+1}$ with $p = 1.5$. For comparison, we also plot the distribution of a thermal plasma with $\langle\gamma\rangle = 1.1\times10^5$ as the dashed line.

How does the resulting energy spectra depend on γ_0, σ_0 and λ? Earlier numerical simulations [20] are limited to regimes with $\gamma_0 \leq 375$. However, global models [16, 35] have suggested a much larger γ_0 and wider range of σ_0. Thanks to our advances in numerical scheme [31] that substantially reduces the growth of numerical instabilities, we are able to explore a much larger range of

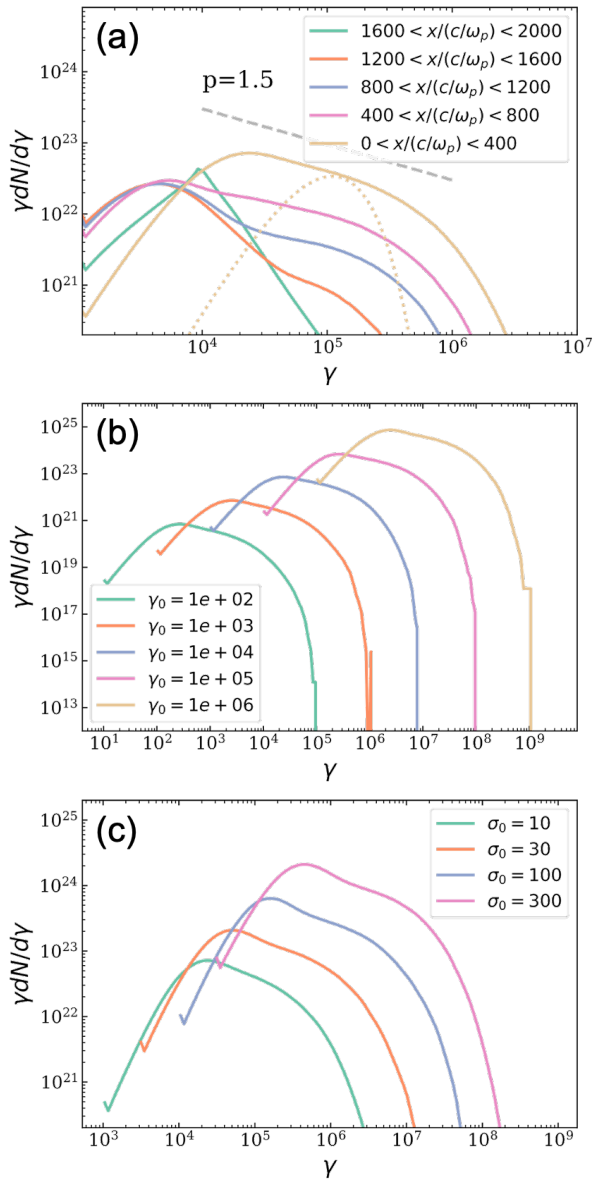

Figure 4. Particle energy distribution $\gamma dN/d\gamma$ for all the electrons and positrons in different regions and different runs (a) At $\omega_p t = 2000$ for the standard run S0. The dashed line is the relativistic thermal distribution for the downstream with peak at $\gamma_0(1+\sigma_0) = 1.1 \times 10^5$. (b) For runs S0, A1, A2, A3, A4 (with different γ_0) in downstream region at time $\omega_p t = 20\sqrt{\gamma_0}$. (c) For runs S0, B1, B2, B3 (with different σ_0) in downstream region at time $\omega_p t = 632\sqrt{\sigma_0}$.

parameters. For the runs with different γ_0 and σ_0 in the range $10^2 \leq \gamma_0 \leq 10^6$ as shown in Figure 4(b) and in the range $10 < \sigma_0 < 300$ as shown in 4(c), the downstream particle energy distributions are similar to the one in the standard run. We confirmed that the power-law energy distribution is scalable for different γ_0 and σ_0. The particles with energy $0.2 < \gamma/(\gamma_0\sigma_0) < 4$ follow a power-law distribution with $p = 1.5$. For different values of magnetization parameter σ_0 and initial bulk flow Lorentz factor γ_0, the spectra are similar if one plots the spectrum against $\gamma/(\sigma_0\gamma_0)$ and the variables $\lambda/(\sqrt{\sigma}c/\omega_p)$ and α are kept the same for different runs, as shown in Figure 5(a). Despite the wide ranges of γ_0 and σ_0, the dimensionless particle-field equations and the initial conditions are the same, as derived in Appendix B. Thus the solutions, i.e. including the particle and field distributions, between different γ_0 and σ_0 are scalable. The particle spectrum depends on the value of $\lambda/(c/\omega_p)$, as shown in Figure 5(b). While the mean energy per particle does not appreciably vary with λ as shown by the red line in the subpanel of Figure 5(b), smaller λ results in narrower spectrum and softer high-energy tail. The ratio $\gamma_{\rm max}/\gamma_{\rm min}$ increases as λ increases and is significantly larger than unity for $\lambda \gtrsim 40d_e$. The power law spectrum forms for the runs with $\lambda \gtrsim 40d_e$. This is similar to the previous study [20] and will be further explained in Section V.

The power-law distribution is stable as long as the shock is well developed and separated from the boundary. The lower bound energy $\varepsilon_{\rm lb}$ and the maximum energy $\varepsilon_{\rm max}$ scale with γ_0 and σ_0 as $\varepsilon_{\rm lb} = 0.2\gamma_0\sigma_0$ and $\varepsilon_{\rm max} = 4\gamma_0\sigma_0$. The maximum energy for electrons and positrons can reach hundreds of TeV ($\gamma > 2 \times 10^8$) for the run with $\gamma_0 \approx 10^6$ and $\sigma_0 = 10$. The power-law distribution of the particles suggests that an acceleration mechanism is very efficient at energizing particles, which will be analyzed and discussed in Section V.

V. PARTICLE ACCELERATION MECHANISM

In order to understand the particle acceleration mechanism at the termination shock of the striped wind, we adopt several techniques for analyzing the results of the standard run, including the particle trajectory, decomposing the particle energization $\boldsymbol{J}\cdot\boldsymbol{E}$ term, and the acceleration rate binned by particle kinetic energy for distinguishing different acceleration mechanisms. With these analyses, we find that the major acceleration mechanism is a Fermi-type acceleration. In the past, the diagnostics for understanding particle acceleration often relies on a few hand-selected particles. Our analysis not only includes particle trajectories but also statistically evaluate the acceleration rate in a quantitative way, so we can evaluate competitive processes without biases.

In Figure 6, we show the trajectories for two typical tracer particles in the simulation. Many of the trajectories we get from the standard run are Fermi-like especially for those accelerated to very high energies, i.e. particles bouncing back and forth and gaining energy. The most important acceleration location is not at the reconnection X-points, but by the relativistic flows generated during magnetic reconnection. As shown in Figure 3(d), the energization rate $\boldsymbol{J}\cdot\boldsymbol{E}$ near the X-points is relatively small compared to that in the reconnection islands, which indicates that Fermi acceleration is more important than

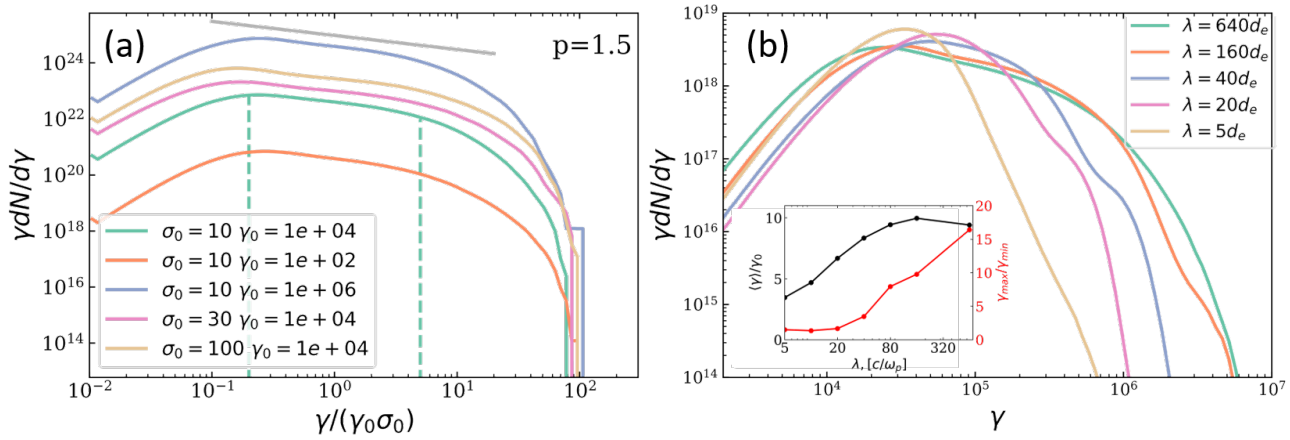

Figure 5. Particle energy distribution $\gamma dN/d\gamma$ for electrons and positrons in different runs (a) For runs S0, A2, A4, B1, B2 in downstream region at time $\omega_p t = 6.32\sqrt{\gamma_0\sigma_0}$. Note that the horizontal axis is $\gamma/(\sigma_0\gamma_0)$ and the vertical dashed lines are at $\gamma/(\gamma_0\sigma_0) = 0.2$ and $\gamma/(\gamma_0\sigma_0) = 4$. (b) For runs S0, C1, C2, C3 (with different wavelength λ) in downstream region. In the subpanel, the black line shows the average Lorentz factor of downstream particles for different λ, the red line presents $\gamma_{\rm max}/\gamma_{\rm min}$ for different λ, where $\gamma_{\rm min}$ is defined as the γ where $\gamma dN/d\gamma$ peaks and $\gamma_{\rm max}$ is defined as the γ where $\gamma^2 dN/d\gamma$ peaks.

direct acceleration at X-line. Once a particle travels into the downstream region of the shock it rarely travels back into the upstream region, indicating that Fermi mechanism in the reconnection islands is also much more efficient than the diffusive shock acceleration at least for the parameter regime we explore in this paper. The acceleration pattern from particle trajectories is distinctly different from earlier work by Sironi and Spitkovsky [20], who concluded that direct acceleration by non-ideal electric field at X-points is the main acceleration mechanism.

To distinguish the relative importance of Fermi acceleration and direct acceleration, we present a number of analyses to statistically evaluate the two mechanisms. The Fermi-type acceleration is mainly through the electric field induced by bulk plasma motion, or more generally, the electric field perpendicular to the local magnetic field, whereas the direct acceleration is driven by the non-ideal electric field, or parallel electric field if a non-zero magnetic field exists. One can distinguish the two mechanisms by calculating the statistical motion of the charged particles and the energization from different components of electric fields. The generalized Fermi acceleration in the relativistic reconnection layer [25, 32, 36] follows the particle journey through a sequence of local frames where local electric field vanishes. For such local frames, we can decompose the electric fields based on Lorentz transformation, with detailed derivations given in the Appendix C 1 and C 2. The ways we decompose the electric fields are a generalization for the non-relativistic case used extensively in previous studies [25, 27, 29, 37]. This generalization is critical in this work because the motion of the bulk flow in our simulations can be highly relativistic. We also calculate the integral of the energization from each term over $0 < x < 1500c/\omega_p$ and $0 < y < 400c/\omega_p$, and compare it with the integral of total energization $P = \int \boldsymbol{J}\cdot\boldsymbol{E}$.

First, we distinguish the electric field associated with bulk plasma motion (motional electric field) from the one that is not (non-ideal electric field). As described in Appendix C 1, we use the following procedures: (1) make a Lorentz boost transforming the electromagnetic field $\boldsymbol{E}$ and $\boldsymbol{B}$ in the simulation frame to $\boldsymbol{E}'$ and $\boldsymbol{B}'$ into the local co-moving frame (the frame moving at $\boldsymbol{\beta}_f c$, where $\boldsymbol{\beta}_f c$ is the speed of the fluid motion), (2) set $\boldsymbol{E}' = 0$ in the co-moving frame, (3) transform the magnetic field $\boldsymbol{B}'$ back into the simulation frame as $\boldsymbol{E}_m$ and $\boldsymbol{B}_m$, where $\boldsymbol{E}_m$ is the electric field due to plasma motion and the remaining part $\boldsymbol{E}_n = \boldsymbol{E} - \boldsymbol{E}_m$ is the non-ideal electric field. In the non-relativistic limit, one obtains $\boldsymbol{E}_m \approx -\boldsymbol{\beta}_f \times \boldsymbol{B}$ and $\boldsymbol{E}_n \approx \boldsymbol{E} + \boldsymbol{\beta}_f \times \boldsymbol{B}$ [29]. The spatial profiles of $\boldsymbol{J}\cdot\boldsymbol{E}_m$ and $\boldsymbol{J}\cdot\boldsymbol{E}_n$ are shown in Figure 7(b) and (c). The profiles of $\boldsymbol{J}\cdot\boldsymbol{E}$ and $\boldsymbol{J}\cdot\boldsymbol{E}_m$ have similar features, both showing different signs on different sides of each island, while $\boldsymbol{J}\cdot\boldsymbol{E}_n$ has smaller value but opposite polarity compared with $\boldsymbol{J}\cdot\boldsymbol{E}_m$. We compare $P_m = \int \boldsymbol{J}\cdot\boldsymbol{E}_m$ with $P = \int \boldsymbol{J}\cdot\boldsymbol{E}$ and find $P_m \approx 0.56P$, which indicates that the motional electric field has a larger contribution to the particle energization than the non-ideal electric field.

The second way to decompose the electric field finds the generalized perpendicular and parallel electric field through a series of frame transformations. As described in Appendix C 2, we use the following procedures: (1) make a Lorentz boost transforming the electromagnetic field $\boldsymbol{E}$ and $\boldsymbol{B}$ in the simulation frame to $\boldsymbol{E}'$ and $\boldsymbol{B}'$ in a local frame where $\boldsymbol{E}'$ and $\boldsymbol{B}'$ are parallel, generally this local frame is also the guiding center frame (2) set $\boldsymbol{E}' = 0$ in that frame, (3) transform the magnetic field $\boldsymbol{B}'$ back into $\boldsymbol{E}_g$ and $\boldsymbol{B}_g$ in the simulation frame. Since $\boldsymbol{E}_g \cdot \boldsymbol{B}_g = 0$ and $(\boldsymbol{E} - \boldsymbol{E}_g) \parallel \boldsymbol{B}_g$, we have the generalized perpendicular electric field $\boldsymbol{E}_\perp = \boldsymbol{E}_g$ and parallel electric

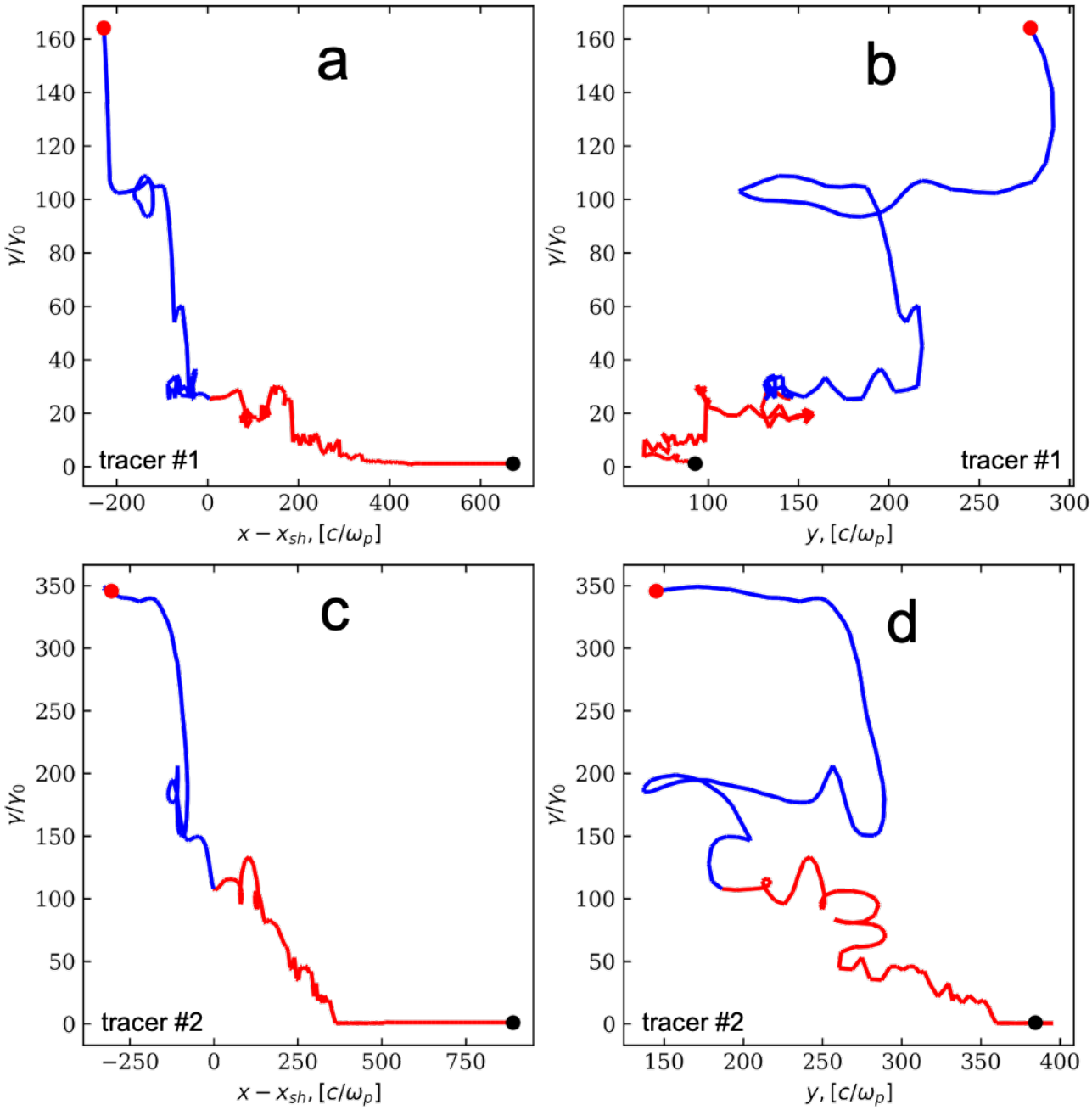

Figure 6. Particle trajectories for two different particles. The left column (a) and (c) is particle Lorentz factor (normalized by γ_0) vs. $x - x_{\rm sh}$ coordinate where the location of the shock jump is approximately at $x_{\rm sh} \approx (ct - 1000c/\omega_p)/3$, and the right column (b) and (d) is particle Lorentz factor (normalized by γ_0) vs. y coordinate. The (a) and (b) are for tracer particle #1, and (c) and (d) are for tracer particle #2. The red line is the trajectory where the particle is in the upstream, and the red line is the trajectory where the particle is in the downstream. The black dots are for particles at $t = 0$, and the red dots are for particles at $\omega_p t = 2000$. The main acceleration process is Fermi-like bounces and particles gain significant amount of energy during each bounce.

field $\boldsymbol{E}_{\parallel} = \boldsymbol{E} - \boldsymbol{E}_g$. In the non-relativistic limit we have $\boldsymbol{E}_{\perp} \approx \boldsymbol{E} - (\boldsymbol{E}\cdot\boldsymbol{B}/B^2)\boldsymbol{B}$ and $\boldsymbol{E}_{\parallel} \approx (\boldsymbol{E}\cdot\boldsymbol{B}/B^2)\boldsymbol{B}$ [25, 27, 37]. The spatial profiles of $\boldsymbol{J}\cdot\boldsymbol{E}_{\perp}$ and $\boldsymbol{J}\cdot\boldsymbol{E}_{\parallel}$ are shown in Figure 7(d) and (e). The spatial profile and amplitude of $\boldsymbol{J}\cdot\boldsymbol{E}_{\perp}$ are similar to that of $\boldsymbol{J}\cdot\boldsymbol{E}$ in Figure 7(a), while $\boldsymbol{J}\cdot\boldsymbol{E}_{\parallel}$ is negligible compared with $\boldsymbol{J}\cdot\boldsymbol{E}_{\perp}$. The integral over $0 < x < 1500c/\omega_p$ for $\boldsymbol{J}\cdot\boldsymbol{E}_{\perp}$ is $P_{\perp} = \int \boldsymbol{J}\cdot\boldsymbol{E}_{\perp} = 0.84P$. The fact that $P_{\parallel} = P - P_{\perp} = 0.16P$ is small indicates that particles gain energy mainly through Fermi-type acceleration.

We also compare the energization rate in $|\boldsymbol{E}| < |\boldsymbol{B}|$

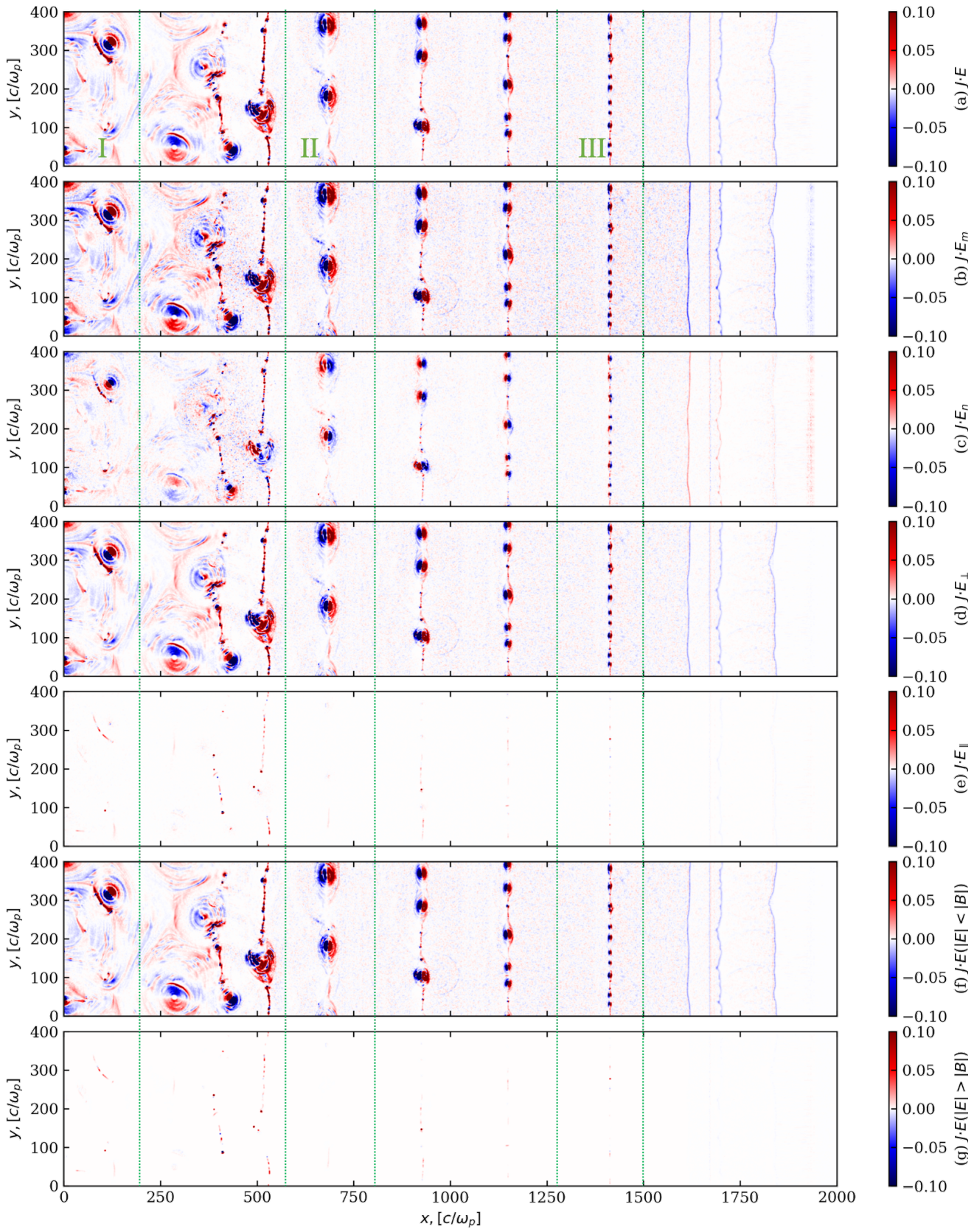

Figure 7. 2D spatial profile for $\boldsymbol{J}\cdot\boldsymbol{E}$ terms in the standard run S0 with $\sigma_0 = 10$, $\gamma_0 = 10^4$, $\alpha = 0.1$ at time $\omega_p t = 2000$. (a) total energization rate $\boldsymbol{J}\cdot\boldsymbol{E}$, (b) $\boldsymbol{J}\cdot\boldsymbol{E}_m$ where $\boldsymbol{E}_m$ is the motional electric field, (c) $\boldsymbol{J}\cdot\boldsymbol{E}_n$ where $\boldsymbol{E}_n$ is the non-ideal electric field, (d) $\boldsymbol{J}\cdot\boldsymbol{E}_\perp$ where $\boldsymbol{E}_\perp$ is the generalized perpendicular electric field, (e) $\boldsymbol{J}\cdot\boldsymbol{E}_\parallel$ where $\boldsymbol{E}_\parallel$ is the generalized parallel electric field, (f) $\boldsymbol{J}\cdot\boldsymbol{E}$ for $|\boldsymbol{E}| < |\boldsymbol{B}|$, (g) $\boldsymbol{J}\cdot\boldsymbol{E}$ for $|\boldsymbol{E}| > |\boldsymbol{B}|$. All the subfigures have the same color scale. $\boldsymbol{J}\cdot\boldsymbol{E}_n$ has smaller value but opposite polarity compared with $\boldsymbol{J}\cdot\boldsymbol{E}_m$. $\boldsymbol{J}\cdot\boldsymbol{E}_\perp$ and $\boldsymbol{J}\cdot\boldsymbol{E}(|\boldsymbol{E}| < |\boldsymbol{B}|)$ are greater than $\boldsymbol{J}\cdot\boldsymbol{E}_\parallel$ and $\boldsymbol{J}\cdot\boldsymbol{E}(|\boldsymbol{E}| > |\boldsymbol{B}|)$.

region and $|\boldsymbol{E}| > |\boldsymbol{B}|$ region in Figure 7(f) and (g) as suggested by Sironi and Spitkovsky [20, 26]. Since $|\boldsymbol{E}|^2 - |\boldsymbol{B}|^2$ is a Lorentz invariant, the decomposition into the $|\boldsymbol{E}| < |\boldsymbol{B}|$ region and the $|\boldsymbol{E}| > |\boldsymbol{B}|$ region are consistent among all the reference frames. Similar to the $\boldsymbol{J} \cdot (\boldsymbol{E} - \boldsymbol{E}_g)$ term, the energization term in $|\boldsymbol{E}| > |\boldsymbol{B}|$ region is negligible. By integrating $\boldsymbol{J} \cdot \boldsymbol{E}$ over subregions where $|\boldsymbol{E}| < |\boldsymbol{B}|$, we find that $P_L = \int_{|\boldsymbol{E}|<|\boldsymbol{B}|} \boldsymbol{J} \cdot \boldsymbol{E} = 0.93P$. The fact that $P - P_L = 0.07P$ is small confirms that the energy conversion from the X-points is much weaker than that in the reconnection islands [27, 29].

We further study the averaged acceleration rate $\langle W \rangle \equiv \langle q\boldsymbol{v} \cdot \boldsymbol{E} \rangle$ for particles of different energy in the simulation at $\omega_p t = 2000$. We show $\langle W \rangle$ in three different regions, in Figure 8(a) and Figure 9(a) for region I ($0 < x < 197c/\omega_p$, where the reconnection islands are in the downstream and already coalesce and grow to large size), in Figure 8(b) and Figure 9(b) for region II ($573c/\omega_p < x < 804c/\omega_p$, where the magnetic islands have a large size but have not yet reached the main shock), and in Figure 8(c) and Figure 9(c) for region III ($1275c/\omega_p < x < 1497c/\omega_p$, where a current sheet just breaks into magnetic islands). Region I is in the downstream of the shock, while region II and III are a pre-shock regions with on-going magnetic reconnection. These regions are also marked as in Figure 3(d) and Figure 7. The averaged acceleration rate is roughly proportional to particle energy over a wide range of energies, indicating that the major acceleration mechanism is Fermi acceleration. The non-ideal electric field $\boldsymbol{E}_n$ only contribute to positive acceleration in a small subset of energy ranges especially in low energies compared to the contribution from the motional electric field $\boldsymbol{E}_m$. The parallel electric field $\boldsymbol{E}_\parallel$ only contribute to positive acceleration in a small subset of energy ranges in high energies compared to the contribution from the motional electric field $\boldsymbol{E}_\perp$.

Theoretical analysis [25, 27, 29] has shown that the power-law of particle spectrum can be explained by solving the energy continuity equation with injection of particles. While Fermi acceleration does not change the shape of the spectrum for the particles in the initial reconnection layer, the injected particles into the layer can form a power law distribution with accelerated energy. In the case of the relativistic striped wind, the injection is continuously going on due to the incoming flow from the striped wind and the particles flowing into the downstream of the shock. The first-order Fermi process, where the acceleration rate is proportional to the energy of the particles as confirmed in Figure 8, is accompanied by the escape of particles from the reconnection islands. In the case of $\lambda = 640d_e$, the spectrum we get from the simulation has $p = 1.5$ as shown in Figure 4, which is consistent with $1 < p < 2$ as we get from the analytical model [25, 27, 29]. In the case of smaller wavelength $\lambda \lesssim 40d_e$ for the striped wind, there are more X-points as the shock-reconnection system evolves. However, the magnetic islands occupy a larger fraction of the total area for a smaller wavelength for the striped wind, resulting in more particles in the initial reconnection layer and less particles injected into the layer. Thus, by applying the theoretical analysis in Guo et al. [25] the particle spectrum are softer and more Maxwellian-like as the wavelength λ decreases, as shown in Figure 5(b).

VI. CONCLUSIONS AND DISCUSSIONS

By carrying out first principles kinetic PIC simulations, we have studied the shock structure and dynamics, magnetic reconnection, and particle energization at the termination shock of a relativistic striped wind. Our parameter regime covers an unprecedented relativistic regime with large bulk Lorentz factor up to $\gamma_0 = 10^6$, which are expected in PWNe. The values of γ_0 and σ_0 are even uncertain for a single PWN, due to the uncertainties in the density at the light cylinder and the global dissipation mechanism in the nebula [16, 35]. For the observed gamma-ray flares [38–42] in the Crab nebula, a sudden drop in the mass loading of the pulsar wind may result in $\sigma_0 \approx 10$ and $\gamma_0 > 10^6$ at the termination shock [35]. The maximum energy for accelerated electrons and positrons can reach hundreds of TeV if $\gamma_0 \approx 10^6$ and $\sigma_0 = 10$. Our study is relevant to magnetic energy conversion and particle acceleration in PWNs produced by oblique rotating pulsars. While a growing body of research using PIC methods focuses on particle acceleration in the spontaneous relativistic magnetic reconnection in the magnetically dominated regime, in this work we extended the study by examining the particle acceleration mechanism in shock driven magnetic reconnection at the termination shock of relativistic striped wind. While the plasma dynamics in this regime is studied extensively by Sironi and Spitkovsky [20], we study carefully the particle energization and acceleration. By analyzing PIC simulations, we found that the termination shock is efficient at converting magnetic energy to particle energy and producing non-thermal power law distributions. The particle distribution is scalable with upstream bulk Lorentz factor γ_0 and magnetization σ_0. For sufficiently large γ_0 and σ_0, the spectrum we get from the simulation has a power law with $p = 1.5$ in energy range $0.2 < \gamma/(\gamma_0\sigma_0) < 4$ for the standard run. Detailed analysis shows that Fermi-type mechanism dominates the particle acceleration and power-law formation. For smaller wavelength ($\lambda \lesssim 40d_e$ for $\sigma_0 = 10$), the spectrum is more Maxwellian-like due to more particles in the initial reconnection layer and less particles injected into the layer.

The high energy particles are known to efficiently produce radiation through a few mechanisms, e.g. synchrotron, bremsstrahlung and inverse-Compton scattering. The morphology of magnetic fields and the spectra of electron-positron pair plasma we get from the PIC simulations can be post-processed to generate the spectrum [43] and polarization [44–46] of the resulting radiation and compared to the observations from the Crab and

other PWNe, which will be subject of future reports.

ACKNOWLEDGEMENTS

Research presented in this paper was supported by the Center for Space and Earth Science (CSES) program and Laboratory Directed Research and Development (LDRD) program 20200367ER of Los Alamos National Laboratory (LANL). The research by PK was also supported by CSES program. The research by YL was supported by CSES student fellowship project. CSES is funded by LANL's LDRD program under project number 20180475DR. FG, PK and HL also acknowledge support from DOE through the LDRD program at LANL and DOE/OFES support to LANL, and NASA Astrophysics Theory Program. The simulations were performed with LANL Institutional Computing which is supported by the U.S. Department of Energy National Nuclear Security Administration under Contract No. 89233218CNA000001, and with the Extreme Science and Engineering Discovery Environment (XSEDE), which is supported by National Science Foundation (NSF) grant number ACI-1548562.

[1] B. M. Gaensler and P. O. Slane, Annual Review of Astronomy and Astrophysics **44**, 17 (2006).

[2] D. F. Torres, *Modelling Pulsar Wind Nebulae* (Springer-Verlag GmbH, 2017), URL `https://www.ebook.de/de/product/30765793/modelling_pulsar_wind_nebulae.html`.

[3] M. J. Rees and J. E. Gunn, Monthly Notices of the Royal Astronomical Society **167**, 1 (1974).

[4] C. F. Kennel and F. V. Coroniti, The Astrophysical Journal **283**, 694 (1984), URL `https://ui.adsabs.harvard.edu/abs/1984ApJ...283..694K`.

[5] C. F. Kennel and F. V. Coroniti, The Astrophysical Journal **283**, 710 (1984), URL `https://ui.adsabs.harvard.edu/abs/1984ApJ...283..710K`.

[6] M. Amenomori, Y. Bao, X. Bi, D. Chen, T. Chen, W. Chen, X. Chen, Y. Chen, Cirennima, S. Cui, et al., Physical Review Letters **123** (2019).

[7] A. U. Abeysekara, A. Albert, R. Alfaro, C. Alvarez, J. D. Álvarez, J. R. A. Camacho, R. Arceo, J. C. Arteaga-Velázquez, K. P. Arunbabu, D. A. Rojas, et al., The Astrophysical Journal **881**, 134 (2019).

[8] A. U. Abeysekara, A. Albert, R. Alfaro, C. Alvarez, J. D. Álvarez, R. Arceo, J. C. Arteaga-Velázquez, D. A. Rojas, H. A. A. Solares, A. S. Barber, et al., Science **358**, 911 (2017).

[9] H. Yuksel, M. D. Kistler, and T. Stanev, Physical Review Letters **103** (2009).

[10] A. Abeysekara, A. Albert, R. Alfaro, J. A. Camacho, J. Arteaga-Velázquez, K. Arunbabu, D. A. Rojas, H. A. Solares, V. Baghmanyan, E. Belmont-Moreno, et al., Physical Review Letters **124** (2020).

[11] L. Accardo, M. Aguilar, D. Aisa, B. Alpat, A. Alvino, G. Ambrosi, K. Andeen, L. Arruda, N. Attig, P. Azzarello, et al., Physical Review Letters **113** (2014).

[12] D. Hooper, I. Cholis, T. Linden, and K. Fang, Physical Review D **96** (2017).

[13] A. A. Abdo, B. Allen, D. Berley, S. Casanova, C. Chen, D. G. Coyne, B. L. Dingus, R. W. Ellsworth, L. Fleysher, R. Fleysher, et al., The Astrophysical Journal **664**, L91 (2007).

[14] T. Linden and B. J. Buckman, Physical Review Letters **120** (2018).

[15] F. V. Coroniti, The Astrophysical Journal **349**, 538 (1990).

[16] J. G. Kirk and O. Skjaraasen, The Astrophysical Journal **591**, 366 (2003).

[17] O. Porth, S. S. Komissarov, and R. Keppens, Monthly Notices of the Royal Astronomical Society **438**, 278 (2014), 1310.2531, URL `https://ui.adsabs.harvard.edu/abs/2014MNRAS.438..278P`.

[18] B. Olmi, L. D. Zanna, E. Amato, and N. Bucciantini, Monthly Notices of the Royal Astronomical Society **449**, 3149 (2015).

[19] O. Porth, M. J. Vorster, M. Lyutikov, and N. E. Engelbrecht, Monthly Notices of the Royal Astronomical Society **460**, 4135 (2016).

[20] L. Sironi and A. Spitkovsky, The Astrophysical Journal **741**, 39 (2011).

[21] G. Giacinti and J. G. Kirk, The Astrophysical Journal **863**, 18 (2018).

[22] L. Sironi, A. Spitkovsky, and J. Arons, The Astrophysical Journal **771**, 54 (2013).

[23] E. J. Summerlin and M. G. Baring, The Astrophysical Journal **745**, 63 (2011).

[24] L. Sironi and A. Spitkovsky, The Astrophysical Journal **698**, 1523 (2009).

[25] F. Guo, H. Li, W. Daughton, and Y.-H. Liu, Physical Review Letters **113** (2014).

[26] L. Sironi and A. Spitkovsky, The Astrophysical Journal **783**, L21 (2014).

[27] F. Guo, Y.-H. Liu, W. Daughton, and H. Li, The Astrophysical Journal **806**, 167 (2015).

[28] F. Guo, X. Li, H. Li, W. Daughton, B. Zhang, N. Lloyd-Ronning, Y.-H. Liu, H. Zhang, and W. Deng, The Astrophysical Journal **818**, L9 (2016).

[29] F. Guo, X. Li, W. Daughton, P. Kilian, H. Li, Y.-H. Liu, W. Yan, and D. Ma, The Astrophysical Journal **879**, L23 (2019).

[30] J. Pétri and Y. Lyubarsky, Astronomy & Astrophysics **473**, 683 (2007).

[31] Y. Lu, P. Kilian, F. Guo, H. Li, and E. Liang, Journal of Computational Physics **413**, 109388 (2020).

[32] M. Lemoine, Physical Review D **99** (2019).

[33] T. D. Arber, K. Bennett, C. S. Brady, A. Lawrence-Douglas, M. G. Ramsay, N. J. Sircombe, P. Gillies, R. G. Evans, H. Schmitz, A. R. Bell, et al., Plasma Physics and Controlled Fusion **57**, 113001 (2015).

[34] B. B. Godfrey, Journal of Computational Physics **15**, 504 (1974).

[35] J. G. Kirk and G. Giacinti, Physical Review Letters **119** (2017).

[36] J. F. Drake, M. Swisdak, H. Che, and M. A. Shay, Nature **443**, 553 (2006).
[37] X. Li, F. Guo, H. Li, and J. Birn, The Astrophysical Journal **855**, 80 (2018).
[38] M. Tavani, A. Bulgarelli, V. Vittorini, A. Pellizzoni, E. Striani, P. Caraveo, M. C. Weisskopf, A. Tennant, G. Pucella, A. Trois, et al., Science **331**, 736 (2011), 1101.2311, URL https://ui.adsabs.harvard.edu/abs/2011Sci...331..736T.
[39] A. A. Abdo, M. Ackermann, M. Ajello, A. Allafort, L. Baldini, J. Ballet, G. Barbiellini, D. Bastieri, K. Bechtol, R. Bellazzini, et al., Science **331**, 739 (2011), 1011.3855, URL https://ui.adsabs.harvard.edu/abs/2011Sci...331..739A.
[40] R. Buehler, J. D. Scargle, R. D. Blandford, L. Baldini, M. G. Baring, A. Belfiore, E. Charles, J. Chiang, F. D. Ammando, C. D. Dermer, et al., The Astrophysical Journal **749**, 26 (2012).
[41] M. C. Weisskopf, A. F. Tennant, J. Arons, R. Blandford, R. Buehler, P. Caraveo, C. C. Cheung, E. Costa, A. de Luca, C. Ferrigno, et al., The Astrophysical Journal **765**, 56 (2013).
[42] R. Buhler and R. Blandford, Reports on Progress in Physics **77**, 066901 (2014).
[43] M. Lyutikov, T. Temim, S. Komissarov, P. Slane, L. Sironi, and L. Comisso, Monthly Notices of the Royal Astronomical Society **489**, 2403 (2019).
[44] A. J. Dean, D. J. Clark, J. B. Stephen, V. A. McBride, L. Bassani, A. Bazzano, A. J. Bird, A. B. Hill, S. E. Shaw, and P. Ubertini, Science **321**, 1183 (2008).
[45] M. Forot, P. Laurent, I. A. Grenier, C. Gouiffès, and F. Lebrun, The Astrophysical Journal **688**, L29 (2008).
[46] E. Jourdain and J.-P. Roques, The Astrophysical Journal **882**, 129 (2019).
[47] A. Galeev, M. Kuznetsova, and L. Zeleny, Space Science Reviews **44** (1986).
[48] W. Daughton, V. Roytershteyn, H. Karimabadi, L. Yin, B. J. Albright, B. Bergen, and K. J. Bowers, Nature Physics **7**, 539 (2011).
[49] L. D. Landau, E. M. Lifshitz, and C. H. Holbrow, Physics Today **16**, 72 (1963).
[50] R. P. Feynman, *Feynman lectures on physics. Volume 2: Mainly electromagnetism and matter* (1964), URL https://ui.adsabs.harvard.edu/abs/1964flp..book.....F.
[51] J. Petri (2019), http://arxiv.org/abs/1910.04591v1.

Appendix A: Test problem with double-periodic box

To make sure the relativistic reconnection onset in our simulations is not due to numerical effects, we carry out several test runs for a current sheet moving in a double-periodic box. The simulation setup is similar to run S0, with $\sigma_0 = 10$, $\alpha = 0.1$, $L_x = \lambda = 640d_e$, $L_y = 400d_e$ and $\Delta = d_e$, except that the x direction is periodic and only covers one wavelength of the striped wind. Therefore, the simulation tests the stability of the striped wind. We use the force interpolation scheme called the WT (standing for **w**eighting with **t**ime-step dependency) scheme proposed in a recent development [31] to overcome the numerical Cherenkov instability (NCI). The WT scheme requires a small time step to improve the numerical stability of the simulations. We test three cases with different time steps $\Delta t = 0.7\Delta t_{\rm CFL}$, $\Delta t = 0.3\Delta t_{\rm CFL}$ and $\Delta t = 0.2\Delta t_{\rm CFL}$, where $\Delta t_{\rm CFL} = 1/(c\sqrt{1/\Delta x^2 + 1/\Delta y^2})$.

The results for the test problem are shown in Figure 10. According to the growth rate of tearing instability given in a previous study [47, 48], the current sheets in the test runs should not reconnect when $\omega_p t$ is a few thousand. Any current sheets reconnect before that time is caused by numerical problems. For the runs with $\Delta t = 0.7\Delta t_{\rm CFL}$ and $\Delta t = 0.3\Delta t_{\rm CFL}$, the reconnection happens before $\omega_p t < 1000$ and the islands have significantly grown their size at $\omega_p t = 2000$, which is roughly the time it takes for the rightmost current sheet to travel before it reaches the main shock. Thus, the results for the runs with $\Delta t = 0.7\Delta t_{\rm CFL}$ and $\Delta t = 0.3\Delta t_{\rm CFL}$ are not consistent with the theoretical prediction. The theoretical prediction [47, 48] is verified using the runs in the co-moving frame of the flow. For the run with $\Delta t = 0.2\Delta t_{\rm CFL}$, the current sheets have not significantly change their morphology from the initial condition until $\omega_p t = 2000$. Since the run with $\Delta t = 0.2\Delta t_{\rm CFL}$ is the most stable run in Figure 10, and it can make sure the current sheet is stable before it interacts with the fast shock, we use the small time step $\Delta t = 0.2\Delta t_{\rm CFL}$ in all the production runs shown in the main context.

Appendix B: Scaling equations for relativistic magnetized plasmas

We show that the particle-field equations for relativistic PIC modeling can be written in the dimensionless form with proper normalization. The equations for relativistic PIC modeling in cgs units are

$$\begin{aligned} m_s\frac{d\boldsymbol{u}_s}{dt} &= q_s(\boldsymbol{E} + \frac{\boldsymbol{v}_s}{c}\times\boldsymbol{B}) \\ \frac{d\boldsymbol{x}_s}{dt} &= \boldsymbol{v}_s \\ \frac{\partial\boldsymbol{E}}{\partial t} &= c\nabla\times\boldsymbol{B} - 4\pi\boldsymbol{J} \\ \frac{\partial\boldsymbol{B}}{\partial t} &= -c\nabla\times\boldsymbol{E} \\ \boldsymbol{J} &= \sum_s w_s q_s \boldsymbol{v}_s \end{aligned} \tag{B1}$$

where s stands for s-th quasi-particle and w_s is the weight of s-th pseudo-particle. We introduce the following normalization

$$\begin{gathered} t = \sigma_0^{1/2}\omega_{pe}^{-1}\tilde{t}, \qquad \boldsymbol{x}_s = \sigma_0^{1/2}(c/\omega_p)\tilde{\boldsymbol{x}}, \\ \boldsymbol{u}_s = \sigma_0\gamma_0 c\tilde{\boldsymbol{u}}_s, \qquad \boldsymbol{v}_s = c\tilde{\boldsymbol{v}}_s, \\ m_s = m_e\tilde{m}_s, \qquad q_s = e\tilde{q}_s, \qquad \tilde{w}_s = n_{c0}\tilde{n}, \\ \boldsymbol{E} = \sqrt{4\pi\gamma_0 n_{c0} m_e c^2\sigma_0}\tilde{\boldsymbol{E}} \qquad \boldsymbol{B} = \sqrt{4\pi\gamma_0 n_{c0} m_e c^2\sigma_0}\tilde{\boldsymbol{B}} \end{gathered} \tag{B2}$$

where $\omega_p = \sqrt{4\pi n_{c0} e^2/(\gamma_0 m_e)}$, then we obtain the dimensionless equations

$$\begin{aligned}
\frac{d\tilde{\boldsymbol{u}}_s}{d\tilde{t}} &= \frac{\tilde{q}_s}{\tilde{m}_s}(\tilde{\boldsymbol{E}} + \tilde{\boldsymbol{v}}_s \times \tilde{\boldsymbol{B}}) \\
\frac{d\tilde{\boldsymbol{x}}_s}{d\tilde{t}} &= \frac{\tilde{\boldsymbol{v}}_s}{c} \\
\frac{\partial \tilde{\boldsymbol{E}}}{\partial \tilde{t}} &= \tilde{\nabla} \times \tilde{\boldsymbol{B}} - \sum_s \tilde{w}_s \tilde{q}_s \tilde{\boldsymbol{v}}_s \\
\frac{\partial \tilde{\boldsymbol{B}}}{\partial \tilde{t}} &= -\tilde{\nabla} \times \tilde{\boldsymbol{E}}
\end{aligned} \tag{B3}$$

and

$$\tilde{\boldsymbol{v}} = \frac{1}{\sqrt{1 + 1/(\tilde{u}^2 \gamma_0^2 \sigma_0^2)}} \frac{\tilde{\boldsymbol{u}}}{\tilde{u}} = (1 - \frac{1}{2\tilde{u}^2\gamma_0^2\sigma_0^2} + \mathcal{O}(\frac{1}{\tilde{u}^4\gamma_0^4\sigma_0^4}))\frac{\tilde{\boldsymbol{u}}}{\tilde{u}} \tag{B4}$$

As long as $\gamma_0 \sigma_0 \tilde{u} \gg 1$, Eq(B4) can be well approximated by $\tilde{\boldsymbol{v}} = \tilde{\boldsymbol{u}}/\tilde{u}$, then the dimensionless equations Eq(B3) are the same for different γ_0 and σ_0. For the simulations in this work, in the upstream flow, we have $\tilde{u} = u/(\sigma_0 \gamma_0 c) \approx 1/\sigma_0 \ll 1$, $\tilde{E} \approx \tilde{B} = 1$, and the normalized wavelength $\tilde{\lambda} = \lambda/(\sqrt{\sigma_0} c/\omega_p)$. As long as the $\tilde{\lambda}$ keeps the same, no matter what σ_0 and γ_0 we have, the initial conditions and the solution for Eq(B3) are scalable. One can then use the solution of Eq(B3) to obtain scalable dimensional results using normalization factors from Eq(B2) .

Appendix C: Decomposing electromagnetic fields

The generalized Fermi acceleration [32] follows the particle journey through a sequence of local frames where local electric field vanishes. To find such local frames, we can decompose the electric fields based on Lorentz transformation. We generalize the decomposition in previous studies [25, 27, 29, 37] to the relativistic case, since the bulk flow in this work can be highly relativistic. In Appendix C 1, by removing the electric field in the fluid co-moving frame, we distinguish the electric field associated with bulk plasma motion (motional electric field) from the one that is not (non-ideal electric field). In Appendix C 2, by removing the electric field in the frame where the electric and magnetic fields are parallel, we get the generalized parallel and perpendicular electric fields.

1. Decomposing electromagnetic field in the bulk fluid frame

For convenience, we define the complex vector of electromagnetic field as $\boldsymbol{F} = \boldsymbol{E} + i\boldsymbol{B}$ [49]. The Lorentz transformation for $\boldsymbol{F} = \boldsymbol{E} + i\boldsymbol{B}$ in the simulation frame S to $\boldsymbol{F}' = \boldsymbol{E}' + i\boldsymbol{B}'$ in fluid co-moving frame S_f which moves at speed $\boldsymbol{\beta}_f c$ with respect to S is (see Chapter 26 in 50)

$$\boldsymbol{F}' = (1 - \gamma_f)(\boldsymbol{F} \cdot \boldsymbol{n}_f)\boldsymbol{n}_f + \gamma_f(\boldsymbol{F} - i\boldsymbol{\beta}_f \times \boldsymbol{F}) \tag{C1}$$

where $\boldsymbol{n}_f = \boldsymbol{\beta}_f/\beta_f$ is the direction of $\boldsymbol{\beta}_f$, and $\gamma_f = 1/\sqrt{1-\beta_f^2}$. If we have a field configuration $\boldsymbol{F}'_m$ in S_f frame such that the electric field $\boldsymbol{E}'_m$ is zero and the magnetic field $\boldsymbol{B}'_m$ is same as $\boldsymbol{B}'$, then

$$\begin{aligned}
\boldsymbol{F}'_m &= i\boldsymbol{B}' \\
&= i[(1 - \gamma_f)(\boldsymbol{B} \cdot \boldsymbol{n}_f)\boldsymbol{n}_f + \gamma_f(\boldsymbol{B} - \boldsymbol{\beta}_f \times \boldsymbol{E})]
\end{aligned} \tag{C2}$$

Transform back $\boldsymbol{F}'_m$ into $\boldsymbol{F}_m$ in S frame, we obtain

$$\begin{aligned}
\boldsymbol{F}_m &= (1 - \gamma_f)(\boldsymbol{F}'_m \cdot \boldsymbol{n}_f)\boldsymbol{n}_f + \gamma_f(\boldsymbol{F}'_m + i\boldsymbol{\beta}_f \times \boldsymbol{F}'_m) \\
&= [-\gamma_f^2 \boldsymbol{\beta}_f \times \boldsymbol{B} - (\gamma_f^2 - 1)(\boldsymbol{E} - (\boldsymbol{n}_f \cdot \boldsymbol{E})\boldsymbol{n}_f)] \\
&\quad + i[-\gamma_f^2 \boldsymbol{\beta}_f \times \boldsymbol{E} \\
&\quad + \gamma_f^2(\boldsymbol{B} - (\boldsymbol{B} \cdot \boldsymbol{n}_f)\boldsymbol{n}_f) + (\boldsymbol{B} \cdot \boldsymbol{n}_f)\boldsymbol{n}_f]
\end{aligned} \tag{C3}$$

The real part of $\boldsymbol{F}_m$, i.e. the electric field due to plasma motion, is

$$\begin{aligned}
\boldsymbol{E}_m &= -\gamma_f^2(\boldsymbol{\beta}_f \times \boldsymbol{B} + \boldsymbol{E} - (\boldsymbol{n}_f \cdot \boldsymbol{E})\boldsymbol{n}_f) + (\boldsymbol{E} - (\boldsymbol{n}_f \cdot \boldsymbol{E})\boldsymbol{n}_f) \\
&= \frac{(\boldsymbol{\mathcal{P}} \cdot \boldsymbol{E})\boldsymbol{\mathcal{P}} - \mathcal{P}^2 \boldsymbol{E} - (\mathcal{E}/c)\boldsymbol{\mathcal{P}} \times \boldsymbol{B}}{(\mathcal{E}/c)^2 - \mathcal{P}^2} \\
&= \frac{\boldsymbol{\mathcal{P}} \times [\boldsymbol{\mathcal{P}} \times \boldsymbol{E} - (\mathcal{E}/c)\boldsymbol{B}]}{(\mathcal{E}/c)^2 - \mathcal{P}^2}
\end{aligned} \tag{C4}$$

where $\boldsymbol{\mathcal{P}}$ is the momentum density of the fluid and $\mathcal{E}$ is the energy density of the fluid, and the fluid velocity is given by $\boldsymbol{\beta}_f c = \boldsymbol{\mathcal{P}} c^2/\mathcal{E}$. In the case where $\beta_f \ll 1$, we have $\boldsymbol{E}_m \approx -\boldsymbol{\beta}_f \times \boldsymbol{B}$.

2. Decomposing electromagnetic field in a frame where electric and magnetic fields are parallel

A frame where the electric and magnetic fields are parallel can be generally found for given electromagnetic field $(\boldsymbol{E}, \boldsymbol{B})$ as long as $E^2 + B^2 > 0$, even for the $B = 0$ case. The velocity $\boldsymbol{v}_g = \boldsymbol{\beta}_g c$ of such frame is given by (see 51 or Section 25 in 49)

$$\frac{\boldsymbol{\beta}_g}{1 + \beta_g^2} = \frac{\boldsymbol{E} \times \boldsymbol{B}}{E^2 + B^2} \tag{C5}$$

where $\boldsymbol{\beta}_g$ and the corresponding Lorentz factor γ_g can be solved as

$$\boldsymbol{\beta}_g = \frac{2\boldsymbol{E} \times \boldsymbol{B}}{E^2 + B^2 + \sqrt{(E^2 - B^2)^2 + 4|\boldsymbol{E} \cdot \boldsymbol{B}|^2}} \tag{C6}$$

$$\gamma_g^2 = \frac{E^2 + B^2 + \sqrt{(E^2 - B^2)^2 + 4|\boldsymbol{E} \cdot \boldsymbol{B}|^2}}{2\sqrt{(E^2 - B^2)^2 + 4|\boldsymbol{E} \cdot \boldsymbol{B}|^2}} \tag{C7}$$

The electromagnetic field $(\boldsymbol{E}, \boldsymbol{B})$ in the simulation frame is transformed into the electromagnetic field $(\boldsymbol{E}', \boldsymbol{B}')$ in frame S_g through a Lorentz transformation using $\boldsymbol{v}_g$. In frame S_g, the electromagnetic field $(\boldsymbol{E}', \boldsymbol{B}')$

satisfies $\boldsymbol{E}' \parallel \boldsymbol{B}'$ and the particle motion follows an accelerating motion in $\boldsymbol{B}'$ direction and a gyro-motion perpendicular to $\boldsymbol{B}'$ direction.

The complex scalar

$$\boldsymbol{F}^2 = \boldsymbol{F}\cdot\boldsymbol{F} = (E^2 - B^2) + 2i\boldsymbol{E}\cdot\boldsymbol{B} = C_R + iC_I \quad \text{(C8)}$$

is a Lorentz invariant, where $C_R = E^2 - B^2$ and $C_I = 2\boldsymbol{E}\cdot\boldsymbol{B}$ [49]. The Lorentz transform for $\boldsymbol{F}$ in the simulation frame S to $\boldsymbol{F}' = \boldsymbol{E}' + i\boldsymbol{B}'$ in a frame S' that moves at speed $\boldsymbol{\beta}_g c$ with respect to S is

$$\boldsymbol{F}' = (1-\gamma_g)(\boldsymbol{F}\cdot\boldsymbol{n}_g)\boldsymbol{n}_g + \gamma_g(\boldsymbol{F} - i\boldsymbol{\beta}_g\times\boldsymbol{F}) \quad \text{(C9)}$$

where $\boldsymbol{n}_g = \boldsymbol{\beta}_g/\beta_g$ is the direction of $\boldsymbol{\beta}_g$. If we define a field configuration $\boldsymbol{F}'_g$ in S' frame such that the electric field $\boldsymbol{E}'_g$ is zero and the magnetic field $\boldsymbol{B}'_g$ is same as $\boldsymbol{B}'$, then by transforming back $\boldsymbol{F}'_g$ into $\boldsymbol{F}_g$ in S frame, we obtain

$$\begin{aligned}\boldsymbol{F}_g &= \gamma_g[\boldsymbol{F}'_a + i\boldsymbol{\beta}_g\times\boldsymbol{F}'_a]\\ &= -\gamma_g^2\boldsymbol{\beta}\times(\boldsymbol{B} - \boldsymbol{\beta}_g\times\boldsymbol{E}) + i\gamma_g^2(\boldsymbol{B} - \boldsymbol{\beta}_g\times\boldsymbol{E})\\ &= (\frac{1}{2} - \frac{C_R}{2\sqrt{C_R^2+C_I^2}} + \frac{C_I i}{2\sqrt{C_R^2+C_I^2}})(\boldsymbol{E} + i\boldsymbol{B})\end{aligned} \quad \text{(C10)}$$

or

$$\begin{aligned}\boldsymbol{E}_g &= (\frac{1}{2} - \frac{C_R}{2\sqrt{C_R^2+C_I^2}})\boldsymbol{E} - (\frac{C_I}{2\sqrt{C_R^2+C_I^2}})\boldsymbol{B}\\ \boldsymbol{B}_g &= (\frac{1}{2} - \frac{C_R}{2\sqrt{C_R^2+C_I^2}})\boldsymbol{B} + (\frac{C_I}{2\sqrt{C_R^2+C_I^2}})\boldsymbol{E}\end{aligned} \quad \text{(C11)}$$

Since $\boldsymbol{E}_g\cdot\boldsymbol{B}_g = 0$ and $(\boldsymbol{E} - \boldsymbol{E}_g) \parallel \boldsymbol{B}_g$, we have the generalized perpendicular electric field $\boldsymbol{E}_\perp = \boldsymbol{E}_g$ and generalized parallel electric field $\boldsymbol{E}_\parallel = \boldsymbol{E} - \boldsymbol{E}_g$. In the case where $|\boldsymbol{E}| \ll |\boldsymbol{B}|$ we have $|C_I/C_R| \approx 2\boldsymbol{E}\cdot\boldsymbol{B}/B^2 \ll 1$ and $C_R < 0$, thus the transformation is equivalent to removing the parallel electric field and keeping the perpendicular electric field

$$\begin{aligned}\boldsymbol{E}_\perp \approx& \boldsymbol{E} - \frac{\boldsymbol{E}\cdot\boldsymbol{B}}{B^2}\boldsymbol{B}\\ \boldsymbol{E}_\parallel \approx& \frac{\boldsymbol{E}\cdot\boldsymbol{B}}{B^2}\boldsymbol{B}\\ \boldsymbol{B}_g \approx& \boldsymbol{B}\end{aligned} \quad \text{(C12)}$$

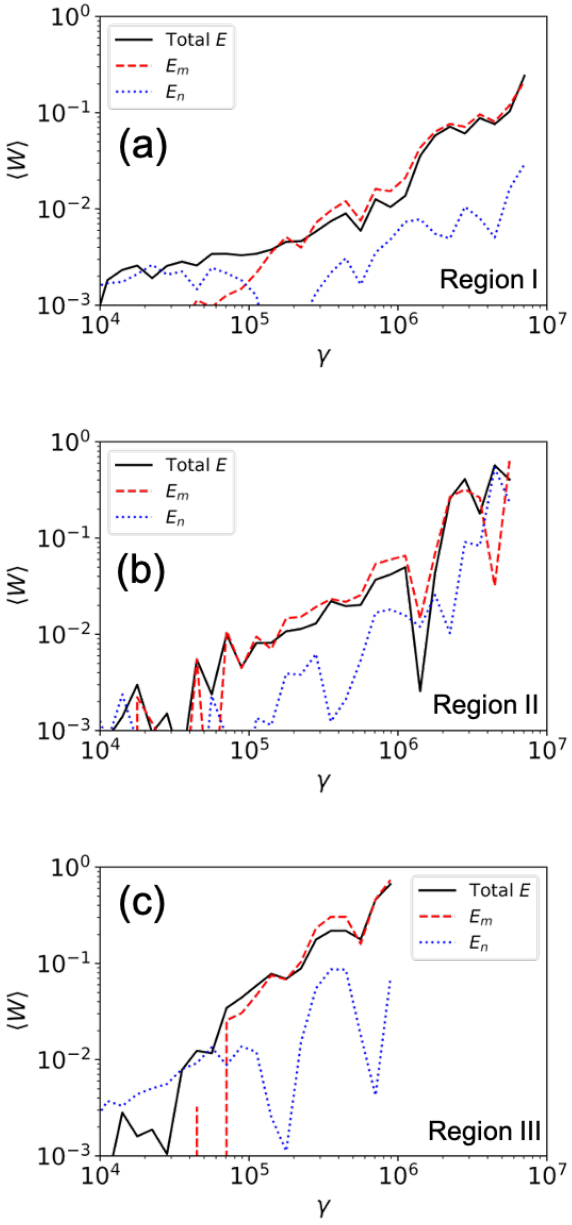

Figure 8. (a) Acceleration rate by total electric field $\boldsymbol{E}$, motional electric field $\boldsymbol{E}_m$ and non-ideal electric field $\boldsymbol{E}_n$ for particles at different energy for $0 < x < 197c/\omega_p$, i.e. region I in Figure 7, at $\omega_p t = 2000$. Note that the curve for $E - E_m$ is the absolute value. (b) same as (a) but for $573c/\omega_p < x < 804c/\omega_p$, i.e. region II in Figure 7. (c) same as (a) but for $1275c/\omega_p < x < 1497c/\omega_p$, i.e. region III in Figure 7. $\boldsymbol{E}_n$ only contributes to positive acceleration in a small subset of energy ranges especially in low energies compared to the contribution from $\boldsymbol{E}_m$.

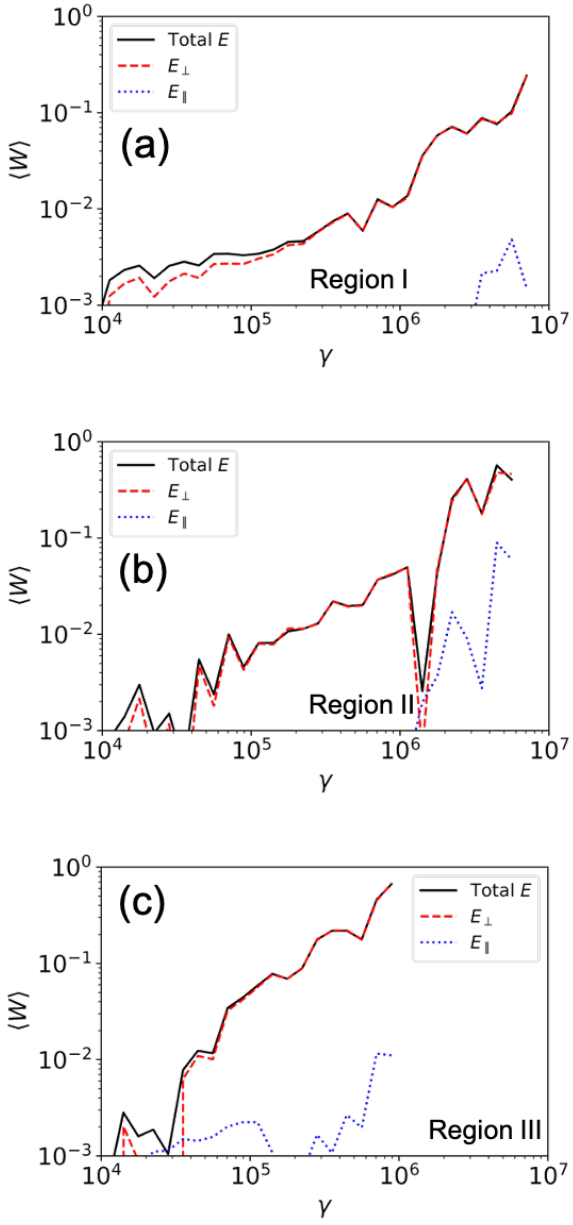

Figure 9. Same as Figure 8 but for the generalized perpendicular electric field $\boldsymbol{E}_\perp$ and parallel electric field $\boldsymbol{E}_\parallel$. $\boldsymbol{E}_\parallel$ only contributes to positive acceleration in a small subset of energy ranges in high energies compared to the contribution from $\boldsymbol{E}_\perp$.

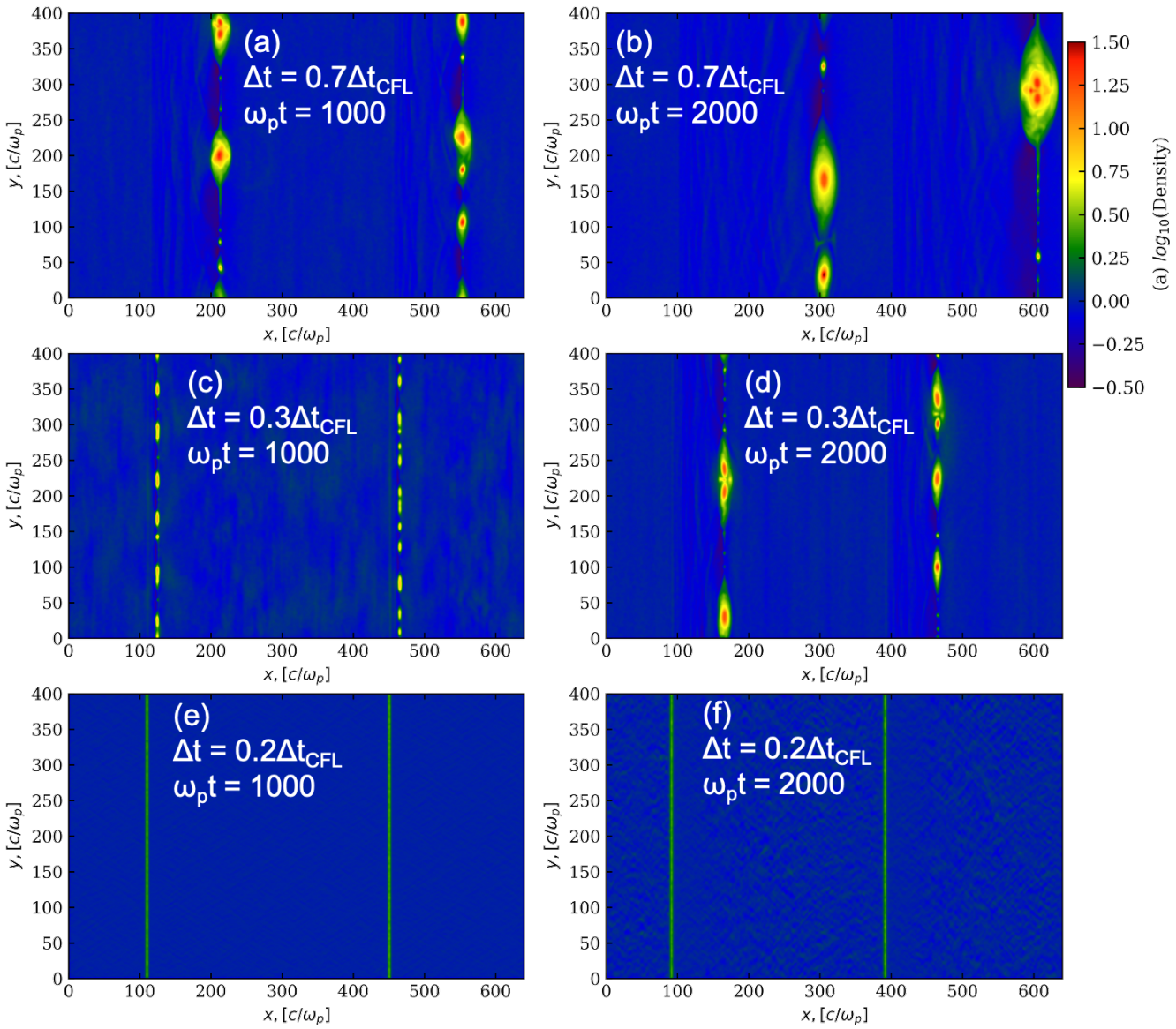

Figure 10. The results for the test problem with $\Delta = d_e$, $L_x = \lambda = 640d_e$ and $L_y = 400d_e$ using double-periodic box. The variable plotted is $\log_{10}(n/n_{c0})$. Subfigures (a), (c) and (e) are at $\omega_p t = 1000$, and subfigures (b), (d) and (f) are at $\omega_p t = 2000$. For different time steps, $\Delta t = 0.7\Delta t_{\rm CFL}$ in (a) and (b), $\Delta t = 0.3\Delta t_{\rm CFL}$ in (c) and (d), and $\Delta t = 0.2\Delta t_{\rm CFL}$ in (e) and (f). The maximum stable time step under the CFL condition is given by $\Delta t_{\rm CFL} = 1/(c\sqrt{1/\Delta x^2 + 1/\Delta y^2})$.